


The lethal K18-hACE2 knock-in mouse model mimicking the severe pneumonia of COVID-19 is practicable for antiviral development

Zhen Zhang^{a,b,*}, Li Zhou^{a,b,*}, Qianyun Liu^{a,*}, Yucheng Zheng^a, Xue Tan^a, Zhixiang Huang^{a,b}, Ming Guo^a, Xin Wang^a, Xianying Chen^a, Simeng Liang^a, Wenkang Li^a, Kun Song^a, Kun Yan^a, Jiali Li^a, Qiaohong Li^{a,b}, Yuzhen Zhang^{a,b}, Shimin Yang^a, Zeng Cai^{a,b}, Ming Dai^b, Qiaoyang Xian^b, Zheng-Li Shi^c, Ke Xu^{a,b}, Ke Lan^{a,b} and Yu Chen ^{a,b}

^aState Key Laboratory of Virology, Modern Virology Research Center and RNA Institute, College of Life Sciences and Frontier Science Center for Immunology and Metabolism, Wuhan University, Wuhan, People's Republic of China; ^bInstitute for Vaccine Research, Animal Bio-Safety Level III Laboratory / Center for Animal Experiment, Wuhan University School of Medicine, Wuhan, People's Republic of China; ^cCAS Key Laboratory of Special Pathogens, Wuhan Institute of Virology, Chinese Academy of Sciences, Wuhan, People's Republic of China

ABSTRACT

Animal models of COVID-19 facilitate the development of vaccines and antivirals against SARS-CoV-2. The efficacy of antivirals or vaccines may differ in different animal models with varied degrees of disease. Here, we introduce a mouse model expressing human angiotensin-converting enzyme 2 (ACE2). In this model, ACE2 with the human cytokeratin 18 promoter was knocked into the Hpp11 locus of C57BL/6J mouse by CRISPR – Cas9 (K18-hACE2 KI). Upon intranasal inoculation with high (3×10^5 PFU) or low (2.5×10^2 PFU) dose of SARS-CoV-2 wildtype (WT), Delta, Omicron BA.1, or Omicron BA.2 variants, all mice showed obvious infection symptoms, including weight loss, high viral loads in the lung, and interstitial pneumonia. 100% lethality was observed in K18-hACE2 KI mice infected by variants with a delay of endpoint for Delta and BA.1, and a significantly attenuated pathogenicity was observed for BA.2. The pneumonia of infected mice was accompanied by the infiltration of neutrophils and pulmonary fibrosis in the lung. Compared with K18-hACE2 Tg mice and HFH4-hACE2 Tg mice, K18-hACE2 KI mice are more susceptible to SARS-CoV-2. In the antivirals test, REGN10933 and Remdesivir had limited antiviral efficacies in K18-hACE2 KI mice upon the challenge of SARS-CoV-2 infections, while Nirmatrelvir, monoclonal antibody 4G4, and mRNA vaccines potently protected the mice from death. Our results suggest that the K18-hACE2 KI mouse model is lethal and stable for SARS-CoV-2 infection, and is practicable and stringent to antiviral development.

ARTICLE HISTORY Received 9 January 2024; Revised 14 April 2024; Accepted 3 May 2024

KEYWORDS SARS-CoV-2; mouse model; K18-hACE2 knock-in mouse; severe pneumonia; Omicron; antivirals

Introduction


Severe acute respiratory syndrome coronavirus 2 (SARS-CoV-2), which caused the coronavirus disease 2019 (COVID-19) pandemic, continues to mutate and spread worldwide, as evidenced by references [1–4], and new SARS-CoV-2 variants are constantly emerging. Most COVID-19 patients have mild symptoms and a satisfactory prognosis at clinical presentation. Unfortunately, some patients may rapidly progress to severe syndromes, such as pneumonia, acute respiratory distress syndrome (ARDS), and multiple organ failure, which can lead to patient death [5,6]. According to autopsy and biopsy reports, most COVID-19 deaths were due to pneumonia and/or ARDS [7–10]. Cytokine and chemokine storms are also associated with severe COVID-19 [11]. Thus, it is a priority for

the global research community to investigate the specific pathogenesis of severe COVID-19 and develop drugs and vaccines to reduce COVID-19 morbidity and mortality.

Suitable animal models are essential for COVID-19 research. Although hamster [12,13], ferret [14], tree shrew [15], and non-human primate [16,17] models have been evaluated for SARS-CoV-2 infection, the SARS-CoV-2 pathogenicity within these animal models ranges only from mild to moderate viral disease. Compared with these animal models, mouse models have the desirable features of tractability: ease of use, high availability, and cost-efficiency. Thus, mouse models that can replicate the severe disease phenotypes and lethal clinical courses observed in COVID-19 patients are still highly needed.

CONTACT Ke Xu  xuke03@whu.edu.cn; Ke Lan  klan@whu.edu.cn; Yu Chen  chenyu@whu.edu.cn  State Key Laboratory of Virology, Modern Virology Research Center and RNA Institute, College of Life Sciences and Frontier Science Center for Immunology and Metabolism, Wuhan University, Luojia Mountain, Wuchang District, Wuhan, 430072 People's Republic of China

*Authors contributed equally: Zhen Zhang, Li Zhou, and Qianyun Liu.

 Supplemental data for this article can be accessed online at <https://doi.org/10.1080/22221751.2024.2353302>.

© 2024 The Author(s). Published by Informa UK Limited, trading as Taylor & Francis Group, on behalf of Shanghai Shangyixun Cultural Communication Co., Ltd. This is an Open Access article distributed under the terms of the Creative Commons Attribution-NonCommercial License (<http://creativecommons.org/licenses/by-nc/4.0/>), which permits unrestricted non-commercial use, distribution, and reproduction in any medium, provided the original work is properly cited. The terms on which this article has been published allow the posting of the Accepted Manuscript in a repository by the author(s) or with their consent.

Conventional laboratory mouse strains have limited syndrome with SARS-CoV-2 infection due to incompatibilities between the mouse angiotensin-converting enzyme 2 (mACE2) ortholog and the SARS-CoV-2 S protein [18]. Currently, several mouse models are under development to overcome this species barrier. The strategies include (1) the exogenous delivery of human *ACE2* (*hACE2*) with a replication-deficient viral vector [19–21]; (2) the expression of *hACE2* as a transgene driven by heterologous gene promoters [21–32]; (3) the expression of *hACE2* driven by the mouse *Ace2* (*mAce2*) promoter [33,34]; and (4) the adaptation of mouse-adapted SARS-CoV-2 [35–38]. While all these mouse models support SARS-CoV-2 infection, mice exogenously transfected with *hACE2* [19,20], expressing *hACE2* under the *mAce2* promoter [33,34], or infected with mouse-adapted SARS-CoV-2 [35,36,38] showed only mild to moderate disease with slight weight loss, reduced lung pathology, and few lethal phenotypes. The mouse model expressing *hACE2* under a lung-ciliated epithelial cell HFH4 promoter (HFH4-*hACE2*) presented significant variations in the infection, mortality, and body weight changes against a high-dose SARS-CoV-2 wildtype (WT) virus challenge (3×10^4 TCID₅₀) [25]. Additionally, a K18-*hACE2* transgenic mouse model (B6.Cg-Tg(K18-*ACE2*)2Prln/J, K18-*hACE2* Tg) that was first generated for studying SARS-CoV [39] was also widely used for evaluating SARS-CoV-2 infection. However, in K18-*hACE2* Tg mice, *hACE2* insertion occurs randomly, which, in turn, may affect the integrity and expression pattern of the *hACE2* and cause the disease severity to vary between individuals in this mouse model (Table S1). In addition, K18-*hACE2* Tg mice require a high-dose SARS-CoV-2 WT virus challenge for 100% lethality to be induced (1×10^5 TCID₅₀ or more) [21,24,28,40].

Recently, it was confirmed that Omicron variants are less pathogenic than previous variants [41–45]. The infection of K18-*hACE2* Tg mice with Omicron variants could potentially result in an overestimation of the efficacy of anti-SARS-CoV-2 drugs and vaccines when evaluating their protective effects. Thus, a more sensitive and stable lethal mouse model is required to replicate the severe respiratory symptoms of COVID-19.

In the present study, we introduced a novel K18-*hACE2* knock-in (KI) mouse model, in which the human *ACE2* gene driven by the human K18 promoter was knocked into the mice's *Hipp11* locus 9 positions. We systematically compare the symptoms of the SARS-CoV-2 infection among K18-*hACE2* KI, K18-*hACE2* Tg, and HFH4-*hACE2* Tg mice. The pathogenesis of SARS-CoV-2 WT, Delta, and Omicron variants has been evaluated in K18-*hACE2* KI mice. Meanwhile, the applicability of this mouse model in anti-SARS-CoV-2 drug development has also been tested.

Results

The comparison of the three *hACE2* mouse models for SARS-CoV-2 infection

The K18-*hACE2* KI mice were generated using CRISPR-Cas9 technology. The human *ACE2* gene driven by the human *K18* promoter was knocked into the *Hipp11* locus on chromosome 11 of the mice, a “genomic safe harbor” for gene knock-in (Figure 1A). Before the infection experiment, we measured the distribution of *hACE2* in heterozygous K18-*hACE2* KI mice. We found that *hACE2* was widely distributed in a variety of tissues, including the eye, brain, nasal turbinate (NT), trachea, lung, heart, liver, intestine, kidney, spleen, and testis of the K18-*hACE2* KI mice. The *hACE2* levels in these tissues ranged from 10^3 to 10^7 copies/mg, and the *hACE2* in the lung and the brain was up to 10^5 copies/mg, consistent with the Western blotting result (Figure 1B and S1A).

To evaluate the susceptibility to SARS-CoV-2, 12-18-week-old male K18-*hACE2* KI mice, along with male K18-*hACE2* Tg mice and male HFH4-*hACE2* Tg mice, were intranasally (i.n.) inoculated with high dose (3.0×10^5 PFU/mouse) or low dose (2.5×10^2 PFU/mouse) of SARS-CoV-2 WT as indicated in Figure 1C. All the mice were monitored daily for disease symptoms, body weight changes, and survival post-infection. In the low dose groups, all K18-*hACE2* KI mice dramatically lost body weight from 3 days-post-infection (dpi) and died by 7 dpi. Meanwhile, K18-*hACE2* Tg mice experienced different degrees of body weight loss from 6 dpi, among this group, four of six mice recovered, and two of six mice died at dpi 8. For HFH4-*hACE2* Tg mice, slight body weight loss was observed from 9 dpi, and only one of six mice died at dpi 9 with 12% weight loss (Figure 1D,E). In the high dose groups, K18 *hACE2* KI mice dramatically lost body weight from 1 dpi, and all died by 5 dpi. While K18-*hACE2* Tg mice experienced body weight loss from 2 dpi to 8 dpi, and all died by 8 dpi. For HFH4-*hACE2* Tg mice, dramatic body weight loss was observed from 4 dpi, and all mice died at dpi 5 (Figure 1H,I).

Next, we measured the viral loads of SARS-CoV-2 in the lungs and brains of these mice at the endpoint (mice dead or mice's weight reached 80% of starting weight, or at the end of experiments). In the low dose groups, the viral load in the lungs and brains of K18-*hACE2* KI mice was significantly higher than that in K18-*hACE2* Tg mice and HFH4-*hACE2* Tg mice (Figure 1F). In the high dose groups, the viral load in lungs and brains of K18-*hACE2* KI mice was significantly higher than that in HFH4-*hACE2* Tg mice, but similar with K18-*hACE2* Tg mice (Figure 1J).

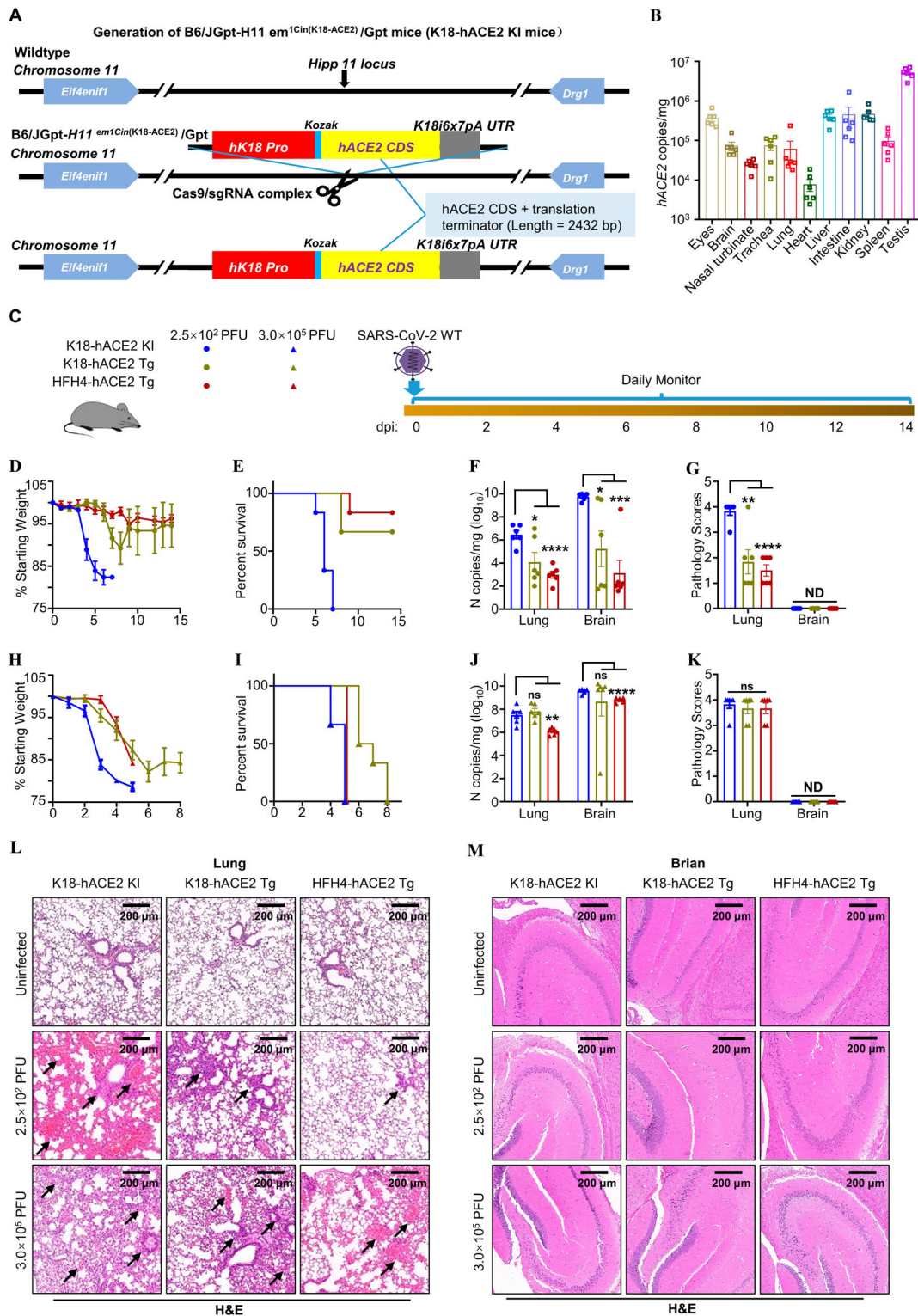


Figure 1. The comparison of outcomes of the hACE2 mouse models to SARS-CoV-2 infection. (A) Generation of K18-hACE2 KI mice. The element containing the K18 promoter, the human ACE2 (hACE2) coding sequence, was inserted into the Hipp11 locus, which can drive the epithelial cell-specific expression of hACE2. (B) hACE2 distribution in the tissues of K18-hACE2 KI mice. K18-hACE2 KI mice ($n = 6$) were euthanized, and the indicated tissues were collected to measure hACE2 mRNA levels via absolute quantification RT-PCR. hACE2 copy numbers were normalized as copies per milligram of tissue. (C) Schematic for SARS-CoV-2 infection. Twelve – to eighteen-week-old K18-hACE2 KI, B6.Cg-Tg(K18-hACE2)2PrImn/J (K18-hACE2 Tg) and HFH4-hACE2 Tg mice were anesthetized, followed by intranasal inoculation with 2.5×10^2 or 3.0×10^5 PFU of SARS-CoV-2 wild-type (WT). Infected mice were monitored and evaluated at the indicated time for (D, H) body weight changes ($n = 6$) and (E, I) survival ($n = 6$), and were then sacrificed to harvest samples at the endpoint of experiment. Mice that lost over 20% of their starting body weight were euthanized. (F, J) Viral N gene copy numbers were measured by absolute quantification RT-PCR in the lungs and the brains. (G, K) Pathology scoring on lung and brain tissues. (L, M) H&E staining of lung and brain tissues obtained from K18-hACE2 KI, K18-hACE2 Tg or HFH4-hACE2 Tg mice following SARS-CoV-2 WT infection. The black arrow indicates the lung tissue damages. One-way ANOVA with Tukey's multiple comparison test was used. ****, $P < 0.0001$; ***, $P < 0.001$; **, $P < 0.01$; *, $P < 0.05$; ns, not significant, $P > 0.05$. Error bars represent the means with SEMs in (B), (D) and (H), and the means with SDs elsewhere. ND, not detected.

Further histological analysis of the lungs was performed, and the infection of low dose SARS-CoV-2 caused severe interstitial pneumonia characterized by a large number of inflammatory cells infiltrating the lungs and the wide thickening and rupture of the alveolar septum in K18-hACE2 KI mice. In contrast, relatively minor lung damages were observed in K18-hACE2 Tg mice and HFH4-hACE2 Tg mice (Figure 1G & 1L). For infection of high dose SARS-CoV-2, severe interstitial pneumonia was observed in all three kinds of tested mice. Interestingly, no obvious pathological phenomenon in brains was detected by H&E staining, no matter the infection dose of SARS-CoV-2 or the kinds of mice (Figure 1K,M).

These results were consistent with the former reports about K18-hACE2 Tg mice (Table S1) and HFH4-hACE2 Tg mice [25], K18-hACE2 KI mice could be killed by as little as 2.5×10^2 PFU of SARS-CoV-2, while limited fatality rates and lung damages were observed in K18-hACE2 Tg mice and HFH4-hACE2 Tg mice, indicating our newly developed K18-hACE2 KI mouse is a lethal model and more susceptible to SARS-CoV-2 infections.

K18-hACE2 KI mice succumbed to the infection of low dose SARS-CoV-2

To further characterize the pathogenesis of SARS-CoV-2 in K18-hACE2 KI mice, we conducted a larger-scale infection experiment with multiple sample collection time points (2, 4, 6 dpi, and endpoint). 12-18-week-old male or female K18-hACE2 KI mice were i.n. inoculated with 3.0×10^5 (high dose) or 2.5×10^2 (low dose) PFU of SARS-CoV-2 WT. All the mice were monitored daily for disease symptoms, body weight changes, and survival post-infection (Figure 2A). The mice infected with 3.0×10^5 PFU SARS-CoV-2 dramatically lost body weight from 1 to 3 dpi, while the mice infected with 2.5×10^2 PFU presented a delayed body weight loss from 3 to 5 dpi. Correspondingly, mice in the high-dose infection group succumbed to infection by 6 dpi, while the mice in the low-dose group died by 7 dpi (Figure 2B,C), and no significant difference was found between male and female K18-hACE2 KI mice in our study (Figure S2).

The viral loads of SARS-CoV-2 in K18-hACE2 KI mice were then measured. We found that SARS-CoV-2 largely accumulated in the lung and brain. As expected, we observed that the viral loads in the lungs of mice infected with 3.0×10^5 PFU of SARS-CoV-2 were significantly higher than those in the group infected with 2.5×10^2 PFU of SARS-CoV-2 at 2 and 4 dpi (Figure 2D). Consequently, the SARS-CoV-2 titer in the lungs of K18-hACE2 KI mice was dependent on the inoculation dose of SARS-CoV-2. In addition, we also found that SARS-CoV-2 could

invade the brains of K18-hACE2 KI mice and that the viral loads in the brains of both groups gradually increased following infection, reaching similar peak titers by 4 dpi (Figure 2E). Unlike that in the lungs, the SARS-CoV-2 titers in the brains of K18-hACE2 KI mice was independent of the inoculation dose. Delayed virus proliferation in the brain may be caused by the blood-brain barrier [46].

To further examine the distribution of SARS-CoV-2 and hACE2 in the K18-hACE2 KI mouse model, we performed an immunofluorescence (IF) analysis on the lungs and brains of mice infected with different doses of SARS-CoV-2. As shown in Figure 2F-I, a large amount of hACE2 (red) was uniformly expressed in the lungs of K18-hACE2 KI mice infected (or not) with SARS-CoV-2. At the same time, the SARS-CoV-2 antigen Nucleocapsid (N protein, green) was only widely expressed in the lungs of mice infected with both a low dose and high dose of SARS-CoV-2; the higher the infectious dose, the greater the SARS-CoV-2 N protein expression (Figure 2F,H). Similarly, we observed that the expression of hACE2 in the brains of infected and uninfected K18-hACE2 KI mice was considerable, while the SARS-CoV-2 N protein was widely expressed in the brains of mice infected with either low or high doses in a manner independent of the infectious dose (Figure 2G,I). These results are consistent with the data shown in Figure 1B, demonstrating that hACE2 is highly expressed in the lung and brain tissues of K18-hACE2 KI mice and that SARS-CoV-2 replicates powerfully in these tissues. Meanwhile, no obvious fluorescence signal of hACE2 had been found in the lung and brain of the normal C57BL/6J mouse (Figure S1B).

To rule out changes in the *hACE2* expression level after virus infection, we also assessed the *hACE2* mRNA levels in the lungs and the brains of infected or uninfected K18-hACE2 KI mice. Compared with uninfected K18-hACE2 mice, the *hACE2* expression level increased in the infected lung (Figure S1C). While there were no significant changes in the brains, no matter the dose for infection (Figure S1D).

These data suggested that SARS-CoV-2 could establish a robust and stable infection and replication in the lungs and brains of K18-hACE2 KI mice, and no matter high or low infection dose, SARS-CoV-2 infection causes a 100% fatality rate.

K18-hACE2 KI mouse model mimics severe pneumonia observed in COVID-19 cases

To investigate the pathological characteristics caused by SARS-CoV-2 infection in the K18-hACE2 KI mouse model, we performed a histopathological analysis on the infected lungs from each group. Using H&E staining analysis indicated that mice

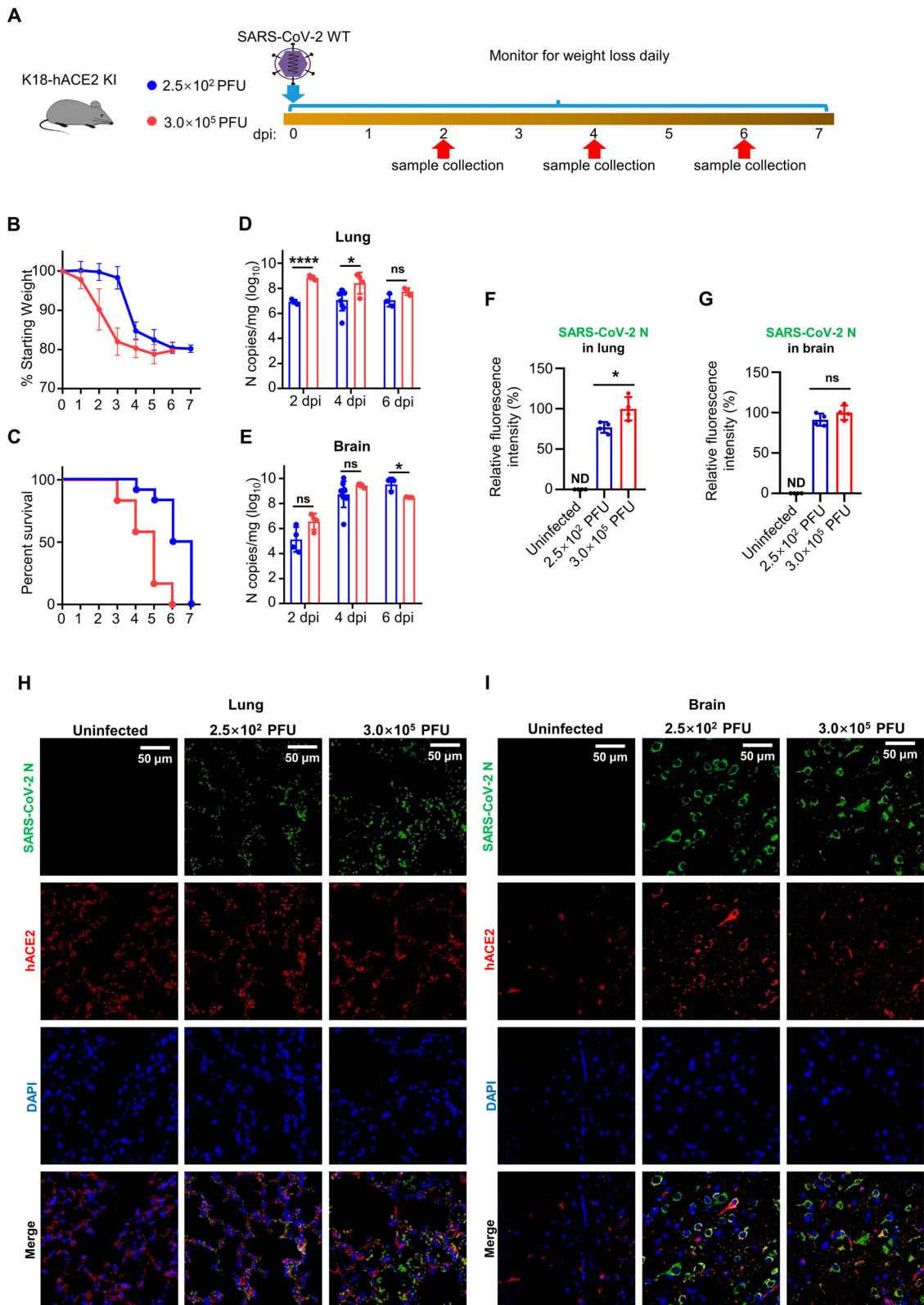


Figure 2. SARS-CoV-2 infection in K18-hACE2 KI results in a lethal infection. (A) Schematic for SARS-CoV-2 infection. Twelve – to eighteen-week-old male and female K18-hACE2 KI mice were anesthetized, followed by intranasal inoculation with 2.5×10^2 or 3.0×10^5 PFU of SARS-CoV-2. Infected mice were monitored and evaluated at the indicated time for (B) body weight changes ($n = 12$) and (C) survival ($n = 12$). At 2, 4, and 6 dpi, at least 3 mice per group were sacrificed to harvest samples, and viral N gene copy numbers in (D) the lungs and (E) the brains were measured by absolute quantification RT-PCR. Mice that lost over 20% of their starting body weight were euthanized. (F) to (I) Immunofluorescence quantification and analysis of hACE2 and SARS-CoV-2 N protein in the lungs and the brains of K18-hACE2 KI mice. In (H) and (I), left panel, the uninfected group; middle panel, the group infected with 2.5×10^2 PFU of SARS-CoV-2 WT at 4 dpi; right panel, the group infected with 3×10^5 PFU of SARS-CoV-2 WT at 4 dpi. Green, SARS-CoV N protein; red, hACE2; blue, DAPI. The scale bar is shown in each section. Two-way ANOVA with Tukey's multiple comparison test was used in (D) and (E), ****, $P < 0.0001$; *, $P < 0.05$; ns, not significant, $P > 0.05$. Unpair Student's t test was used in (F) and (G), *, $P < 0.05$; ns, not significant, $P > 0.05$; ND, not detected. Error bars represent the means with SEMs in (B) and the means with SDs elsewhere.

inoculated with 2.5×10^2 PFU of SARS-CoV-2 presented pneumonia gradually progressing from mild to severe as the infection progressed. At 2 dpi, the mice showed slight lung-tissue damage and peribronchial inflammation with the infiltration of monocytes, neutrophils, and lymphocytes. At 4 dpi, the infiltration of immune cells around the pulmonary blood vessels and alveoli increased significantly. At 6 dpi, most of the alveolar walls had thickened. At the same time, many inflammatory cells appeared around the bronchi and blood vessels, and the lung interstitium was replaced by collagen fibers and fibroblasts (Figure 3A).

In comparison, the mice in the high-dose group (3.0×10^5 PFU) showed more severe lung inflammation than those in the low-dose group (2.5×10^2 PFU), and the infection quickly developed into severe pneumonia (Figure 3A). At 2 dpi, moderate interstitial pneumonia, such as peribronchial and perivascular inflammation with massive cell infiltration, appeared in the lung tissue. At 4 and 6 dpi, a large number of inflammatory cells infiltrated into the lungs, and the alveolar septum widely thickened and ruptured, while peripheral protein exuded in the local tissue, suggesting that inflammation further accumulated in the lung tissue (Figure 3A). These results were consistent with the immunohistochemical analysis of pulmonary fibrosis (Figure 3B) and immunofluorescence analysis of neutrophils (Figure 3C), both of which indicated severe inflammation in the lungs. In summary, after being infected with SARS-CoV-2, K18-hACE2 KI mice can develop severe pneumonia that is similar to the pulmonary disease observed in severe COVID-19 patients.

In addition, we also explored whether SARS-CoV-2 infection could induce encephalitis in K18-hACE2 KI mice. We performed a pathological analysis via H&E staining on the brain tissues of infected mice in both the low- and high-dose groups. Compared with those in the uninfected group, the structures of the brains of mice infected with either low-dose or high-dose virus remained normal, even in the late stage of viral infection, with no apparent pathological phenomenon. The neurons in the CA1 region of the hippocampus of the brain were full, round, and closely arranged (Figure 3D). This result was consistent with the results of neutrophil immunofluorescence, which showed little neutrophil infiltration in the brain tissue (Figure 3E). These results indicate that SARS-CoV-2 can invade the brain; however, the infection did not cause apparent inflammatory injury during the survival times of the mice.

SARS-CoV-2 infection activates the PRRs and interferon-related genes in the lungs and brains of K18-hACE2 KI mice

It is widely reported that SARS-CoV-2 infection can cause severe inflammatory cytokine and chemokine

storms in COVID-19 patients, especially in severe cases [11]. To investigate the immune responses triggered by SARS-CoV-2 in this lethal K18-hACE2 KI mouse model, we measured the mRNA levels of pattern recognition receptors (PRRs), interferons, cytokines, and chemokines in both the lungs and brains of K18-hACE2 KI mice.

As shown in Figure 4A, in the lung tissue, Toll-like receptors (such as *Tlr3*, *Tlr7*, and *Tlr8*), RIG-I-like receptors (such as *Ddx58*), and interferon regulatory factors (such as *Irf7*) were upregulated after infection. Meanwhile, we noticed that the interferon-related-signalling pathways in mice infected with high-titer virus (3.0×10^5 PFU) were more potently activated than those in the low-dose infection group (2.5×10^2 PFU) in the early infection stage (2 dpi). Unexpectedly, we found that only a minority of interferons (*Ifnb* and *Ifnl2/3*) were induced, other interferons remained in a resting state or gradually decreased with the progress of viral infection.

In the brains, a similar result was observed with minor differences. The mRNA levels of genes upstream of the interferons, such as *Tlr3*, *Tlr7*, *Ddx58*, and *Irf7*, were upregulated to some extent at 4 and 6 dpi. In response, only the *Ifnb* mRNA level was insignificantly upregulated in the high-dose infection group (Figure 4B). However, the level of interferon responses induced by SARS-CoV-2 between the low-dose group and the high-dose group showed no significant differences, which meant that the interferon responses in the brain were not closely correlated with the initial inoculation dose of SARS-CoV-2.

SARS-CoV-2 infection is prone to inducing inflammatory cytokine-related genes in the lungs instead of the brains in K18-hACE2 KI mice

To investigate the local inflammatory responses induced by SARS-CoV-2 in the K18-hACE2 KI mouse model, we compared the levels of several typical inflammatory cytokines in both the lungs and brains of infected and uninfected mice. As shown in Figure 5A, the mRNA levels of *Il1b*, *Tnfa*, *Il12a*, *Il10*, *Il6*, *Il1a*, and *Il17f* were upregulated in the lungs of SARS-CoV-2-infected mice. As the viral infection progressed, inflammatory cytokines including *Il1b*, *Tnfa*, and *Il12a* peaked at 6 dpi, at which point the mice either died from SARS-CoV-2 infection or arrived at the endpoint of the experiment. Moreover, the levels of inflammatory cytokines (*Il1b*, *Tnfa*, *Il12a*, and *Il1a*) in the lungs of mice infected with high-dose viruses were significantly higher than those in the low-dose group. Interestingly, some anti-inflammatory cytokines (*Il10* and *Il6*) and Th17 cytokines (*Il17a* and *Il17f*) were only considerably upregulated in the group infected with 2.5×10^2 PFU of SARS-CoV-2 at 2 dpi and, afterward, decreased to background levels at 4 and 6 dpi (Figure 5A). By contrast,

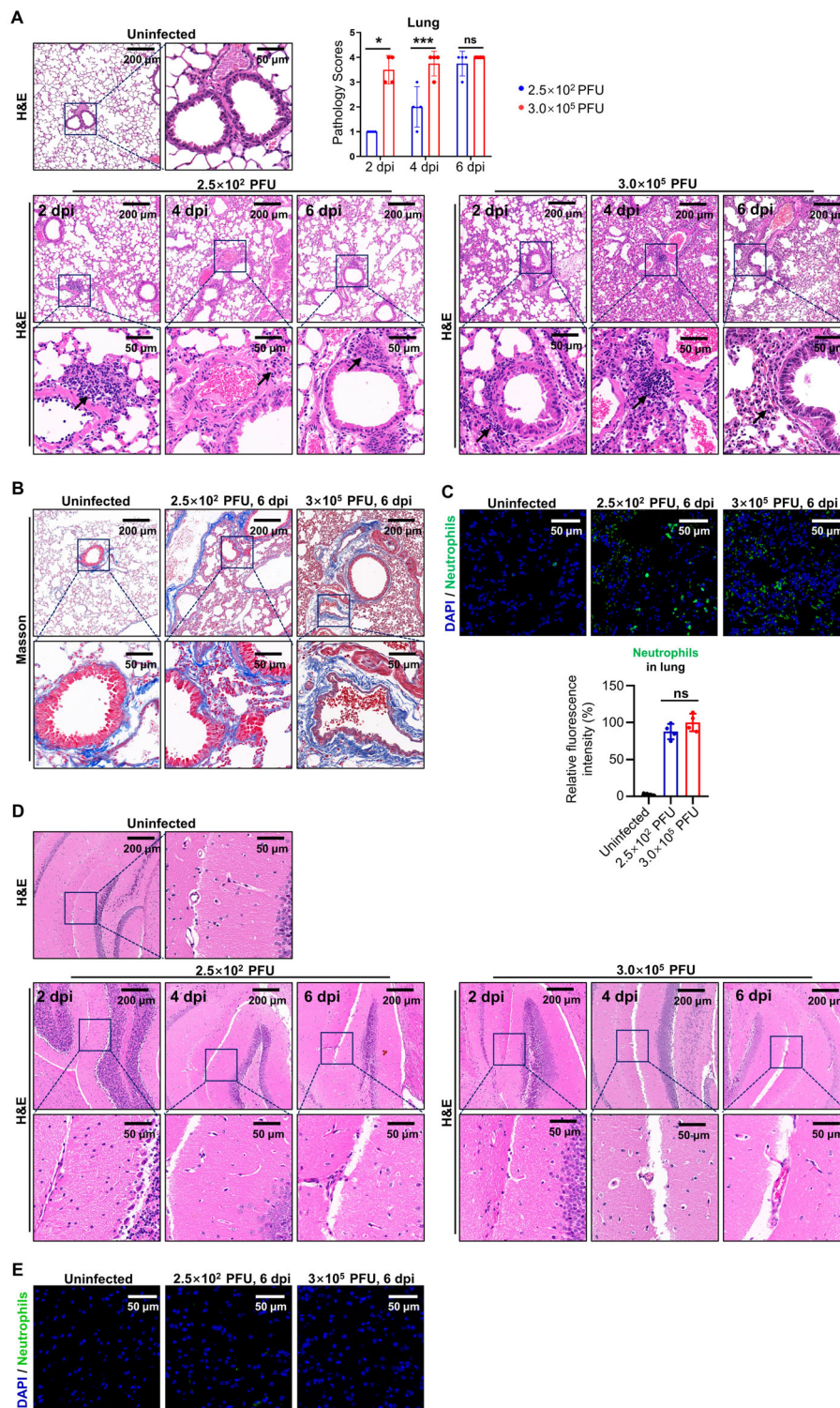


Figure 3. Lung and brain histopathological analysis of K18-hACE2 KI mice. (A) Lung H&E staining of K18-hACE2 KI mice and the pathology scores. The lungs of K18-hACE2 KI mice collected at 2, 4, and 6 dpi were subjected to H&E staining. The uninfected mice served as the control group. The black arrow indicates the lung tissue damages. (B) IHC analysis for pulmonary fibrosis in SARS-CoV-2-infected mice. Pulmonary fibrosis was marked with Masson (blue). Left panel, the uninfected group; middle panel, the group infected with 2.5×10^2 PFU of SARS-CoV-2 WT at 6 dpi; right panel, the group infected with 3×10^5 PFU of SARS-CoV-2 WT at 6 dpi. (C) Lung immunofluorescence analysis and quantification for neutrophils (Neu⁺) in SARS-CoV-2-infected mice. Neutrophils are marked with Ly6G. Left panel, the uninfected group; middle panel, the group infected with 2.5×10^2 PFU of SARS-CoV-2 at 6 dpi; right panel, the group infected with 3×10^5 PFU of SARS-CoV-2 at 6 dpi. Blue, DAPI; green, Ly6G. The scale bar is shown in each section. (D) Brain H&E staining of K18-hACE2 KI mice. The brains of K18-hACE2 KI mice collected from the indicated time point were subjected to H&E staining. The uninfected mice served as the control group. (E) The brain immunofluorescence analysis for neutrophils (Neu⁺) in SARS-CoV-2-infected mice. Neutrophils are marked with Ly6G. Left panel, the uninfected group; middle panel, the group infected with 2.5×10^2 PFU of SARS-CoV-2 at 6 dpi; right panel, the group infected with 3×10^5 PFU of SARS-CoV-2 at 5 dpi. Blue, DAPI; green, Ly6G. The scale bar is shown in each section. ***, $P < 0.001$; *, $P < 0.05$; ns, not significant, $P > 0.05$. Two-way ANOVA with Tukey's multiple comparison test was used in (A), ***, $P < 0.001$; *, $P < 0.05$; ns, not significant, $P > 0.05$. Unpair Student's t test was used in (C), ns, not significant, $P > 0.05$. Error bars represent the means with SDs.

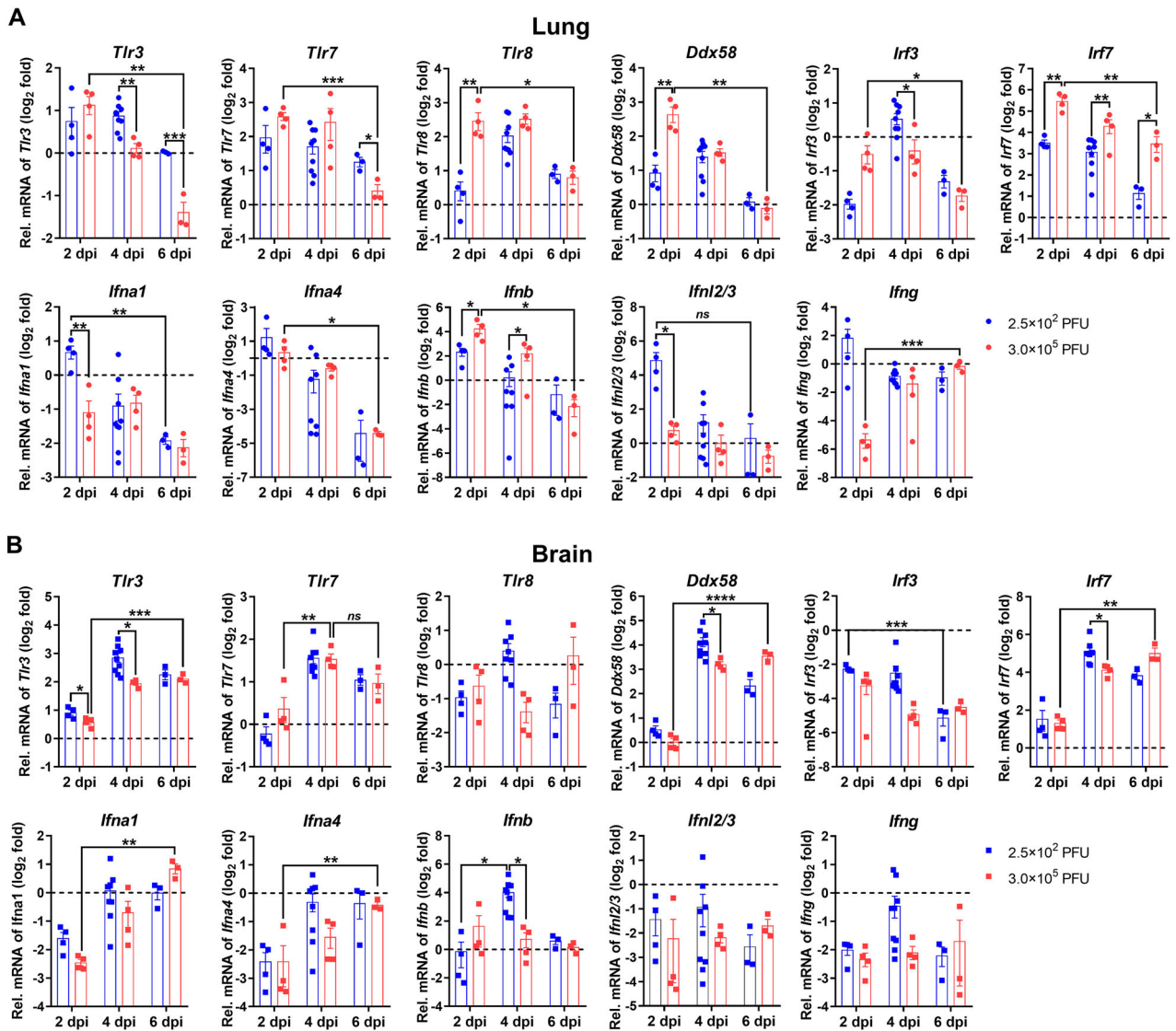


Figure 4. SARS-CoV-2 infection activated PRRs and interferons in K18-hACE2 KI mice. The mRNA levels of *Tlr3*, *Tlr7*, *Tlr8*, *Ddx58*, *Irf3*, *Irf7*, *Ifna1*, *Ifna4*, *Ifnb*, *Ifnl2/3*, and *Ifng* in (A) the lungs and (B) the brains were measured by relative quantification RT-PCR. The results are expressed as fold changes in the gene RNA levels in infected mice relative to the uninfected control. *Gapdh* was used as housekeeping gene. Two-way ANOVA with Tukey's multiple comparison test was used. ****, $P < 0.0001$; ***, $P < 0.001$; **, $P < 0.01$; *, $P < 0.05$; ns, not significant, $P > 0.05$. Error bars represent the means with SEMs.

inflammatory cytokines, including *Tnfa*, *Il1b*, *Il6*, and *Il1a*, were only slightly increased in the brains of K18-hACE2 KI mice at 4 and 6 dpi when compared with the uninfected mice (Figure 5B). These results show that SARS-CoV-2 infection induced observable inflammatory cytokine storms in the lungs but not brains of K18-hACE2 KI mice.

SARS-CoV-2 infection upregulates the chemokine-related genes in the lungs and brains of K18-hACE2 KI mice

We also evaluated the chemokine levels triggered by SARS-CoV-2 in this K18-hACE2 KI mouse model. The inflammatory chemokines *Ccl2*, *Ccl3*, *Ccl4*, *Cxcl1*, *Cxcl2*, *Cxcl5*, *Cxcl9*, and *Cxcl10* were remarkably upregulated in the lungs of infected mice, and the mRNA levels of *Ccl3*, *Ccl4*, *Cxcl2*, *Cxcl9*, and

Cxcl10 were significantly higher in the high-dose infected group (Figure 6A). Interestingly, we found that the mRNA levels of *Ccl2* and *Cxcl1* were lower in the lungs of mice infected with high titers of virus. In the brains, chemokines including *Ccl3*, *Ccl4*, *Ccl5*, *Cxcl9*, and *Cxcl10* were significantly upregulated at 4 and 6 dpi and remained highly consistent with the viral replication curves in the brains of K18-hACE2 KI mice (Figure 6B). The results show that SARS-CoV-2 induced severe chemokine storms in the lungs and brains of K18-hACE2 KI mice.

The above results indicate that K18-hACE2 KI mice infected with SARS-CoV-2 develop severe inflammatory cytokine and chemokine responses in an infectious-dose-dependent manner in the lung, which is consistent with the pulmonary pathological characteristics. By contrast, the mice showed weak inflammatory cytokine responses but strong chemokine

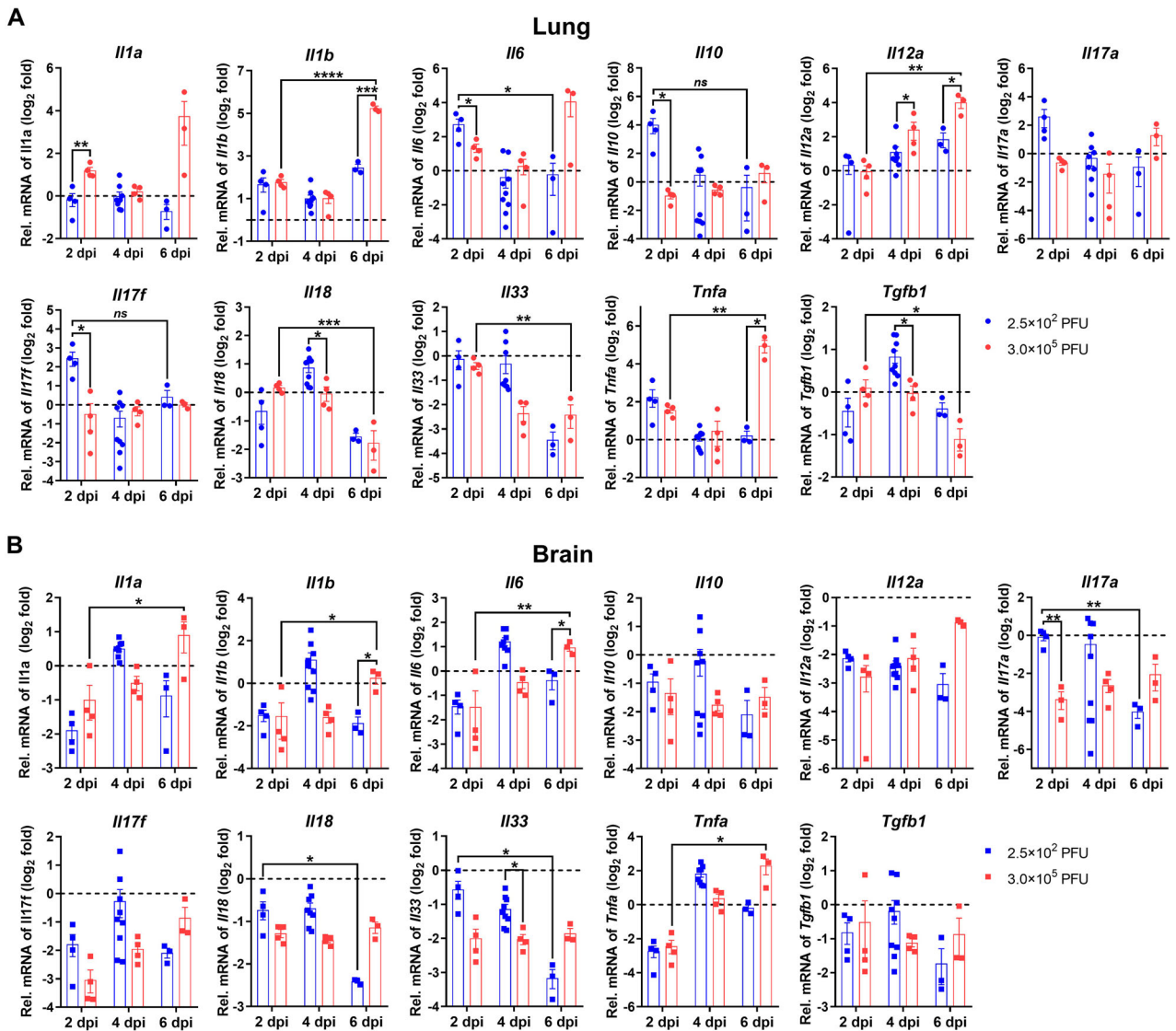


Figure 5. SARS-CoV-2 infection induced inflammatory cytokines in K18-hACE2 KI mice. The mRNA levels of *Il1a*, *Il1b*, *Il6*, *Il10*, *Il12a*, *Il17a*, *Il17f*, *Il18*, *Il33*, *Tnfa*, and *Tgfb1* in (A) the lungs and (B) the brains were measured by relative quantification RT-PCR. The results are expressed as fold changes in the gene RNA levels in infected mice relative to the uninfected control. *Gapdh* was used as housekeeping gene. Two-way ANOVA with Tukey's multiple comparison test was used. ****, $P < 0.0001$; ***, $P < 0.001$; **, $P < 0.01$; *, $P < 0.05$; ns, not significant, $P > 0.05$. Error bars represent the means with SEMs.

responses in an infectious-dose-independent manner in the brain, with no detectable encephalic pathological changes. Considering the morbidity and mortality differences between the K18-hACE2 KI mice infected with high and low doses of SARS-CoV-2, we speculated that tissue-specific pathology and immune responses dominated the severity of the disease in K18-hACE2 KI mice. The lethality of SARS-CoV-2 in K18-hACE2 KI mice was strongly associated with severe pulmonary pathology and inflammatory responses in the lung.

Infection of low dose Delta and Omicron variants induced death in K18-hACE2 KI mice via viral pneumonia

To investigate whether there were differences in the pulmonary pathology and inflammatory responses

caused by different SARS-CoV-2 strains, we inoculated K18-hACE2 KI mice with the SARS-CoV-2 WT, Delta, Omicron BA.1, Omicron BA.2 variants (Figure 7A). The mice infected with 2.5×10^2 PFU of the Delta or Omicron BA.1 variants showed significant body weight loss from 4 dpi, which was about 2 days later compared to that in the mice infected with 2.5×10^2 PFU of WT virus, while the mice infected with 2.5×10^2 PFU of the Omicron BA.2 variant showed significant body weight loss from 6 dpi (Figure 7B). As the infection proceeded, the mice infected with Delta or BA.1 variants all died by 7 dpi or 8 dpi, respectively, while the mice infected with 2.5×10^2 PFU of WT virus all died by 6 dpi. 40% of mice infected with BA.2 variant died by 12 dpi, and the rest survived (Figure 7C). We then measured the viral loads in the lungs and found that the genome copies of SARS-CoV-2 showed no significant

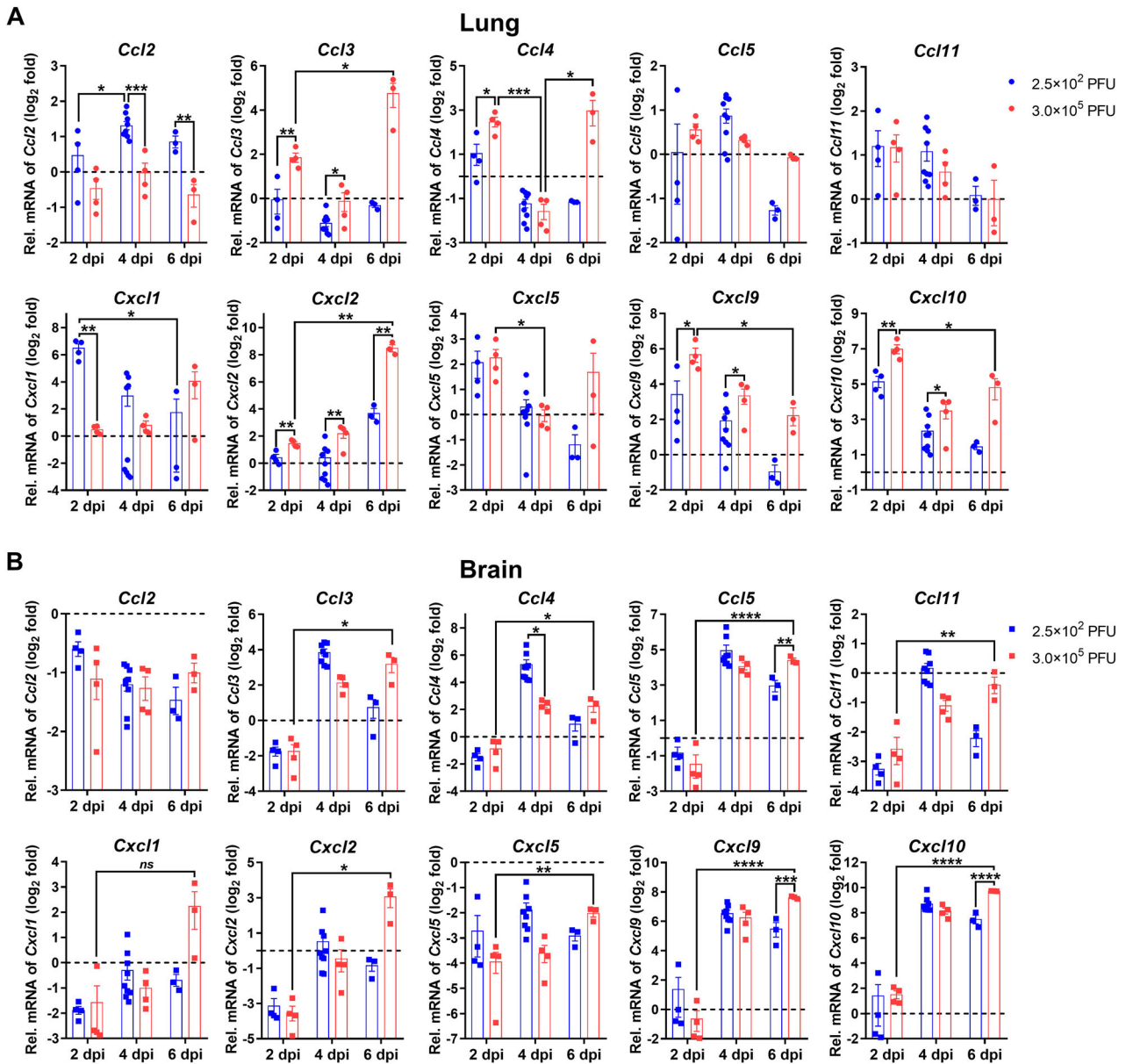


Figure 6. SARS-CoV-2 infection induced chemokine storms in K18-hACE2 KI mice. the mRNA levels of *Ccl2*, *Ccl3*, *Ccl4*, *Ccl5*, *Ccl11*, *Cxcl1*, *Cxcl2*, *Cxcl5*, *Cxcl9*, and *Cxcl10* in (A) the lungs and (B) the brains were measured by relative quantification RT-PCR. The results are expressed as fold changes in the gene RNA levels in infected mice relative to the uninfected control. *Gapdh* was used as housekeeping gene. Two-way ANOVA with Tukey's multiple comparison test was used. ****, $P < 0.0001$; ***, $P < 0.001$; **, $P < 0.01$; *, $P < 0.05$; ns, not significant, $P > 0.05$. Error bars represent the means with SEMs.

differences between these four groups at endpoint (Figure 7D). Pathological analysis found infiltration of monocytes, neutrophils, and lymphocytes around the pulmonary blood vessels and cell degenerations of alveolar walls in both WT, Delta, BA.1, and BA.2 variants at endpoint, but the number of inflammatory cells and the thickness of the alveolar walls in BA.1-infected and BA.2-infected lungs were significantly less than those in WT-infected lungs (Figure 7E,F). This decreasing inflammation is similar to the attenuated pathogenicity of the BA.1 – and BA.2 – infected K18-hACE2 KI mice, which suggests the close relationship between the lethality of SARS-CoV-2 and severe pulmonary pathology and inflammatory responses.

K18-hACE2 KI mice are practicable and stringent to anti-SARS-CoV-2 drug evaluation

To evaluate the potential of K18-hACE2 KI mice in anti-SARS-CoV-2 drug development, four antivirals and one vaccine were tested against the SARS-CoV-2 WT infection in this mouse model: mAb REGN10933 (one of the effective parts of FDA-proved REGN-COV2), mAb 4G4 (a reported human mAb developed from COVID convalescents [47]), Remdesivir (RDV), Nirmatrelvir (NMV), and mRNA vaccine (based on the formulation of mRNA-1273 [48], 1 μ g/mouse). All groups of K18-hACE2 KI mice were i.n. infected with 2.5×10^2 PFU SARS-CoV-2 WT viruses at 0 dpi. In the mAb groups, K18-hACE2 KI mice were intraperitoneally injected with 10 mg/kg REGN10933

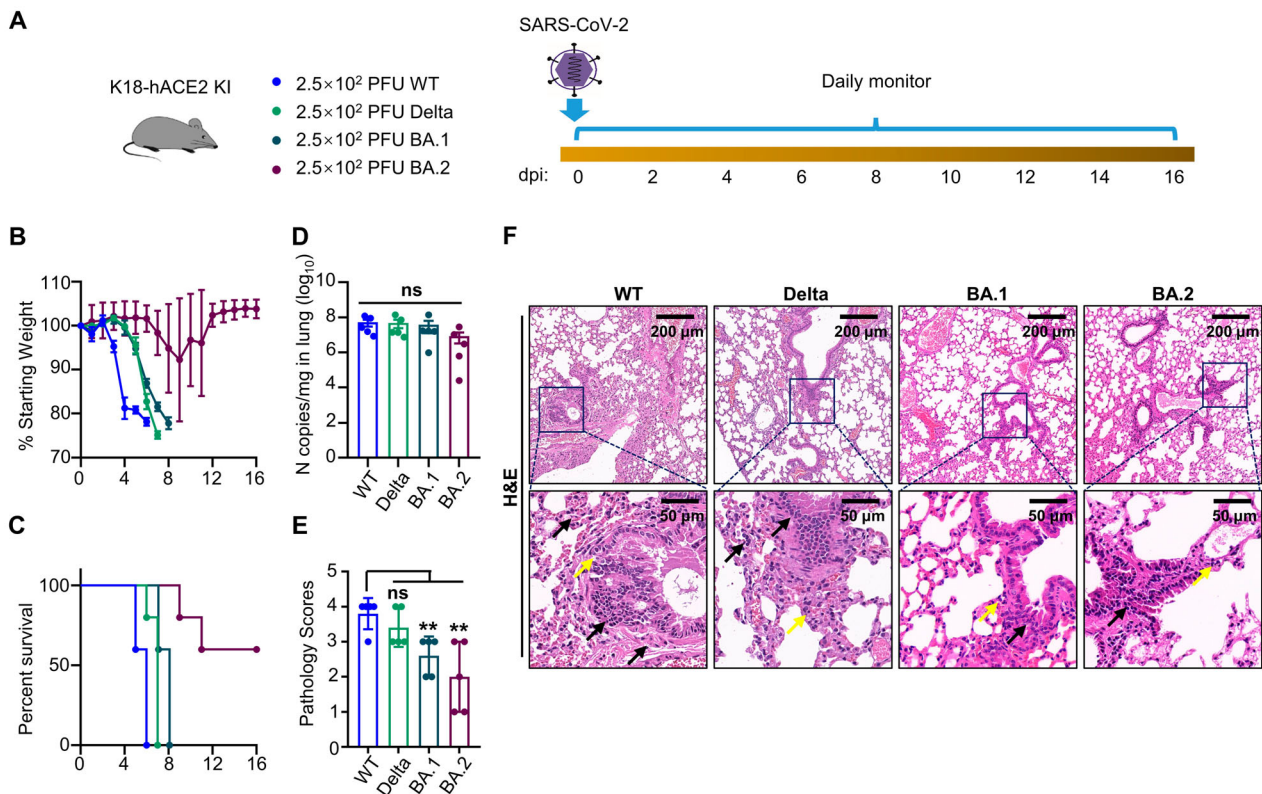


Figure 7. K18-hACE2 KI mouse infection with SARS-CoV-2 variants. (A) Schematic for SARS-CoV-2 infection. Twelve-week-old K18-hACE2 KI mice were i.n. inoculated with 2.5×10^2 PFU of SARS-CoV-2 WT, Delta, Omicron BA.1, or Omicron BA.2 of SARS-CoV-2. Infected mice were monitored and evaluated at the indicated time for (B) body weight changes ($n = 5$) and (C) survival ($n = 5$). At endpoint ($n = 5$), mice were sacrificed to harvest their lungs, and (D) viral N gene copy numbers were measured by absolute quantification RT-PCR. Mice that lost over 20% of their starting body weight were euthanized. Error bars represent the means with SDs. (E) Pathology scores. (F) Lung H&E staining of K18-hACE2 KI mice. The lungs of K18-hACE2 KI mice collected at endpoint were subjected to H&E staining and histology scoring. The scale bar is shown in each section. The black arrow indicates the lung tissue damage, the yellow arrow indicates the infiltration of monocytes. Two-way ANOVA with Tukey's multiple comparison test was used. **, $P < 0.01$; ns, not significant, $P > 0.05$. Error bars represent the means with SEMs in (B) and the means with SDs elsewhere.

or 4G4, respectively at -1 dpi. In the RDV group, mice were treated with 25 mg/kg RDV daily by intraperitoneally injection from 0 to 5 dpi, while 300 mg/kg NMV was administrated daily by oral gavage from 0 to 5 dpi in the NMV group (Figure 8A). In the vaccine group, K18-hACE2 KI mice received the first dose of mRNA vaccine intramuscularly 6 weeks prior to infection, followed by the second dose 3 weeks before infection. Each method of treatment had its own control, and no significant difference was found between these controls (Figure S3). For legibility, we set the mAb control group to be the negative control in Figure 6. The mice from the negative control group and RDV group dramatically lost body weight from 3 dpi, and all succumbed to infection by 8 dpi. Mice treated with REGN10933 dramatically lost body weight from 4 dpi, and 75% of mice succumbed to infection by 8 dpi. Encouragingly, mice treated with 4G4, NMV, or mRNA vaccines all survived, and no significant weight change was observed (Figure 8B,C). The viral loads of SARS-CoV-2 in the lungs of K18-hACE2 KI mice were also determined. REGN10933, 4G4, NMV and vaccines significantly decreased the viral loads in the

lungs compared to the control, while RDV did not show inhibition to the replication of SARS-CoV-2 in lungs (Figure 8D). Lung pathology analysis showed that SARS-CoV-2 caused severe interstitial pneumonia (infiltration of monocytes, neutrophils, and lymphocytes and cell degenerations of alveolar walls) in the negative control group, REGN10933 group, and RDV group. In contrast, only mild lesions were observed in mice injected with 4G4, NMV, or vaccines (Figure 8E,F). Considering the better antiviral effects of REGN10933 and RDV in other SARS-CoV-2 infection models [49–53], our results indicated that the K18-hACE2 KI mouse model is practicable and stringent to anti-SARS-CoV-2 drug developments.

Discussion

Animal models play a crucial role in COVID-19 research. In this study, we present the characteristics of a K18-hACE2 KI mouse strain, where a single-copy K18-hACE2 integration was achieved by inserting the *K18-hACE2* element into the *Hipp11* locus on chromosome 11 in wildtype mice (Figure 1A).

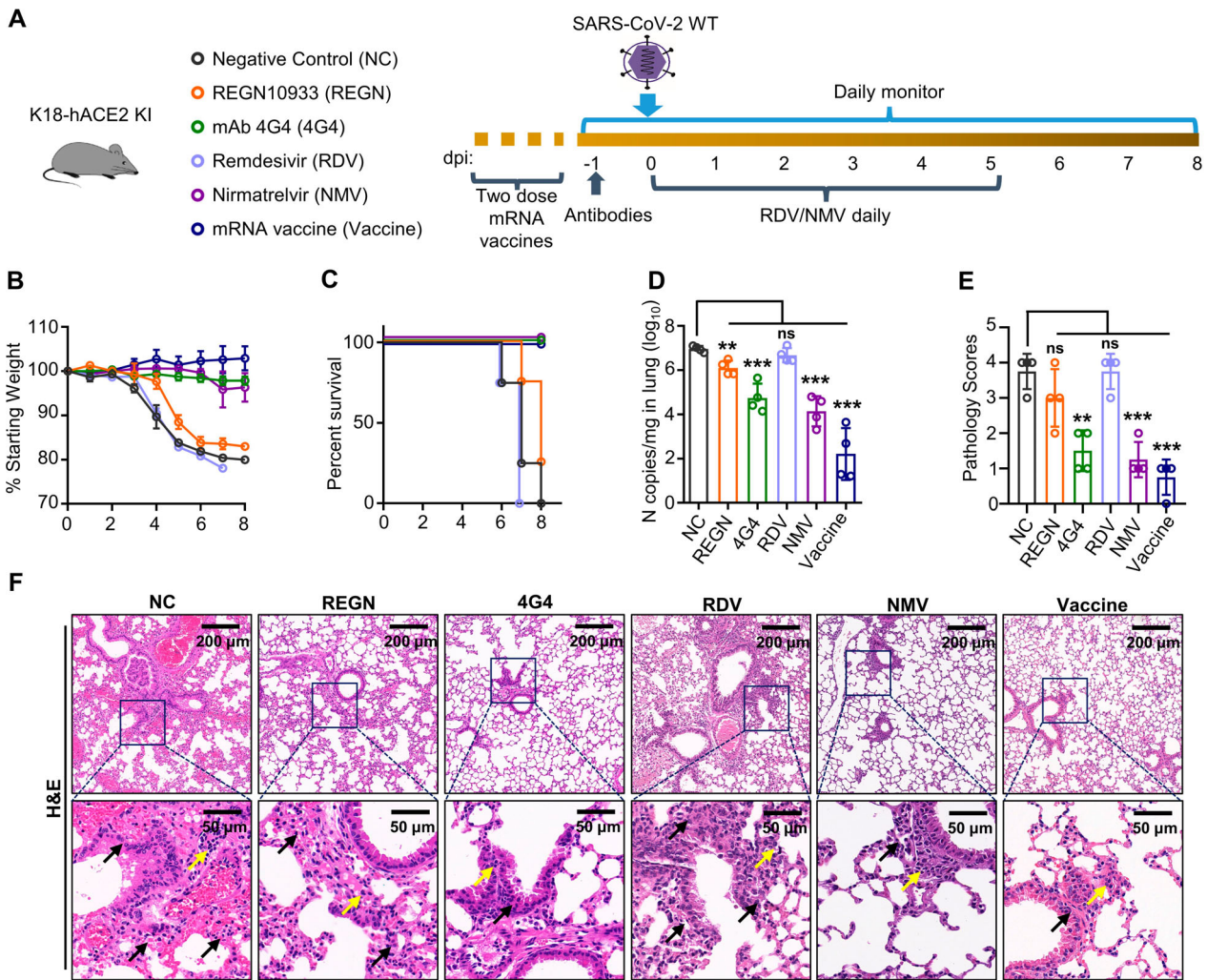


Figure 8. Evaluation of anti-SARS-CoV-2 drug by K18-hACE2 KI mouse model. (A) Schematic of experimental design for anti-SARS-CoV-2 neutralizing antibody, mRNA vaccine, and drug treatment. Twelve-week-old K18-hACE2 KI mice were injected with 10 mg/kg REGN10933 or 4G4 at -1 dpi, or treated with 25 mg/kg Remdesivir (RDV) daily by intraperitoneally injection from 0 to 5 dpi, or treated with 300 mg/kg Nirmatrelvir (NMV) daily by oral gavage from 0 to 5 dpi. For mRNA vaccine, mice received the first dose of mRNA vaccine intramuscularly 6 weeks prior to infection, followed by the second dose 3 weeks before infection. All groups K18-hACE2 KI mice were infected i.n. with 2.5×10^2 PFU SARS-CoV-2 WT viruses at 0 dpi. Mice that lost over 20% of their starting body weight were euthanized. Infected mice were monitored and evaluated at the indicated time for (B) body weight changes ($n = 4$), (C) survival ($n = 4$) and (D) viral N gene copy numbers at experimental endpoint. (E) Pathology scores. (F) The lungs of K18-hACE2 KI mice collected at experimental endpoint were subjected to H&E staining and histology scoring. The scale bar is shown in each section. The black arrow indicates the lung tissue damage, the yellow arrow indicates the infiltration of monocytes. One-way ANOVA with Tukey's multiple comparison test was used. ***, $P < 0.001$; **, $P < 0.01$; ns, not significant, $P > 0.05$. Error bars represent the means with SEMs in (B) and the means with SDs elsewhere.

The *hACE2* was distributed in multiple organs, including the lungs and brains of K18-hACE2 KI mice (Figure 1B), which were shown to be highly susceptible to SARS-CoV-2 inoculation. After infection, these mice showed rapid body weight loss, high viral loads, and 100% mortality (Figures 1 and 2). Further investigation revealed that the SARS-CoV-2 infection of the K18-hACE2 KI mice induced progressive pneumonia, which was evidenced by vasculitis, edema, and injury to parenchymal cells, intra-alveolar fibrin, collagen fibers, and fibroblasts in the lung interstitium (Figure 3). Along with pneumonia, cytokine and chemokine storms (Figures 4 and 5) in the lung exhibited a diverse cellular infiltrate mainly composed of

neutrophils and monocytes (Figure 3). The combination of viral infection and cytokine/chemokine storms in the lung may be the primary cause of severe pneumonia, which mimicked the severe pulmonary disease caused by SARS-CoV-2 in humans [9,10].

An important distinction between our study and others using *hACE2* transgenic mice is that K18-hACE2 KI mice succumbed to 2.5×10^2 PFU inoculation with SARS-CoV-2 WT by 8 dpi (Figures 1, 2, 7, and 8). This lethality rate was not observed in the HFH4-hACE2 Tg mice or K18-hACE2 Tg mice after SARS-CoV-2 infection (Table S1). While *hACE2* is expressed under the same human K18 promoter, the transgene insertion of *hACE2* occurs randomly [39].

Thus, the integrity and cellular expression of hACE2 would probably be affected. As we compared the hACE2 level in the lung and brain between K18-hACE2 KI mice and K18-hACE2 Tg mice, the expression of hACE2 in K18-hACE2 KI mice is significantly higher and more consistent than that in K18-hACE2 Tg mice (Figure S4A-B), which could explain the different mortality doses of SARS-CoV-2. Besides the lung and brain, SARS-CoV-2 can also replicate in the intestine of K18-hACE2 KI mice with very low intensity than in the lung or brain, and no significant damages were observed (Figure S4C-D), indicating that the K18-hACE2 KI mouse model may not be suitable for intestinal infection of COVID-19. We also considered whether this result could have been due to SARS-CoV-2 strain differences. Hence, we assessed the pathogenicity of the Delta, Omicron BA.1, and Omicron BA.2 variants in K18-hACE2 KI mice. We found that both Delta and BA.1 variants (2.5×10^2 PFU) could also cause 100% mortality among K18-hACE2 KI mice, even though the survival times of the mice increased (Figure 7). Meanwhile, no more than 47% mortality of K18-hACE2 Tg mice after 1×10^3 – 2×10^3 PFU Omicron BA.1 infection was reported, without significant body weight loss or severe lung damages [43,44]. A significantly attenuated pathogenicity was observed for BA.2 infection in K18-hACE2 KI mice (Figure 7). Meanwhile, no significant body weight loss or mortality was observed in K18-hACE2 Tg mice after 1×10^3 BA.2 infection [54]. These results suggest that the K18-hACE2 KI mouse model is a stable lethal model for SARS-CoV-2 infection, optimized for studying severe pneumonia, but not suitable for studying persistent infections or Long COVID.

Strikingly, we noticed that the tissue-specific immune responses were closely associated with the local pathology in SARS-CoV-2-infected K18-hACE2 KI mice. Similar to some laboratory investigations on the neuroinvasion of SARS-CoV-2 [21,29,46], we found that SARS-CoV-2 WT could invade the brains of K18-hACE2 KI mice (Figures 1, 2). Even though high viral loads activated PRR signalling, these loads induced mild inflammatory responses in an infectious-dose-independent manner in the brain (Figures 4B and 5B). Meanwhile, minimal histopathological lesions (Figure 3D) or neutrophil infiltration (Figure 3E) were observed in the brains of K18-hACE2 KI mice. By contrast, K18-hACE2 KI mice infected with SARS-CoV-2 WT developed severe lung inflammatory cytokine and chemokine responses and pulmonary pathology in an infectious-dose-dependent manner in the lungs (Figures 3A–C, 4A, 5A, and 6A). Therefore, we hypothesized that this lung-specific pathology and immune response dominated the severity of the disease in K18-hACE2 KI mice. In addition, this hypothesis was supported by the correspondence

between delayed pulmonary inflammation and the delayed death of Delta-, Omicron BA.1-, and Omicron BA.2-infected K18-hACE2 KI mice (Figure 7).

REGN10933, which is one of the effective constituents of REGN-COV2 that has been granted Emergency Use Approval by the U.S. Food and Drug Administration mAbs against COVID-19, has 100% protective efficacy against SARS-CoV-2 in rhesus macaques and hamsters [52,53]. When tested in K18-hACE2 KI mice, REGN10933 still can significantly decrease the viral load in the lungs, but only 25% protection efficacy was observed. While 4G4, with lower EC_{50} than REGN10933 [47], 100% protected K18-hACE2 KI mice against SARS-CoV-2 infections, and no significant syndrome was observed. mRNA vaccines play important roles in the fight against COVID-19, $1 \mu\text{g}/\text{mouse}$ mRNA vaccine also 100% protected K18-hACE2 KI mice against SARS-CoV-2 WT infections, and no significant syndrome was observed (Figure 8). And Remdesivir, which can accelerate virus clearance, and diminished cellular infiltration of lung tissue in infected Ad5-hACE2-transduced mice [50] and K18-hACE2 Tg mice [49], showed limited antiviral efficacy in K18-hACE2 KI mice. The different antiviral efficacy might be related to the higher and more consistent expression of hACE2 in K18-hACE2 KI mice than K18-hACE2 Tg mice. While Nirmatrelvir, the antiviral component of Paxlovid, showed 100% protective efficacy in K18-hACE2 KI mice (Figure 6), consistent with its antiviral efficacy in K18-hACE2 Tg mice [49]. Considering the better clinical therapeutic effect of Paxlovid than Remdesivir [55,56], the different efficacy of REGN10933 and Remdesivir between the K18-hACE2 KI mouse model and other models indicated that the K18-hACE2 KI mouse model is stringent to the drug and vaccine development, and not easily leads to overestimation of antivirals.

hACE2 is abundantly present in the lung, small intestine, and trachea of both humans and K18-hACE2 KI mice [57,58], but a high level of hACE2 is also found in the eye, brain, liver, kidney, and testis of K18-hACE2 KI mice (Figure 1B). Therefore, our findings on antiviral might not fully extrapolate to humans or other animal models. Meanwhile, we acknowledge that the exact cause of death for these K18-hACE2 KI mice upon SARS-CoV-2 infection remains to be determined. One of the possible causes of death is the inflammatory cytokine storms in the lungs, and according to the GO-BP pathway analysis (Figure S5), the regulation of inflammatory response, leukocyte migration, cytokine-mediated signalling pathway, stress-activated MAPK cascade, I-kappaB kinase/NF-kappaB signalling, and JNK cascade were significantly enriched pathways in the lungs of SARS-CoV-2-infected K18-hACE2 KI mice. However, the cause of the tissue-specific inflammatory responses

induced by SARS-CoV-2 in K18-hACE2 KI mice is still unclear. The brain was long considered to be an organ with an immune-privileged status because of its isolation from the immune system by the blood–brain barrier, the lack of draining lymphatics, and the immunoincompetence of microglia and resident macrophages [59]. In recent years, it was demonstrated that brain immune cells can respond to damage and pathogens and initiate proper innate/adaptive immune responses; our research also supports this perspective (Figures 4–6). Brain immune responses play roles in limiting neuronal injury, helping to clear debris from degenerated cells, and restoring the cerebral environment for repair [60]. This is probably why we observed high viral loads but no apparent histopathological lesions in the brains of K18-hACE2 KI mice infected with SARS-CoV-2 WT. The specific mechanism needs to be further studied. Notably, all mice in our experiments were intranasally inoculated with SARS-CoV-2, this way of inoculation could be a potential reason for virus presence in the brain, and different ways of inoculation may cause the change in virulence.

In summary, our study demonstrated that the K18-hACE2 KI mouse model is highly susceptible to intranasal infection with SARS-CoV-2 WT, Delta, and Omicron BA.1 variants (lethal dose $\leq 2.5 \times 10^2$ PFU) and that the lethality of SARS-CoV-2 is closely associated with severe pulmonary pathology and inflammatory responses. Significantly, the pathology observed in the infected mouse model resembled that observed in COVID-19 patients. Thus, the K18-hACE2 KI mouse is an attractive animal model for defining the mechanisms underlying the transmission and pathogenesis of SARS-CoV-2 and understanding the unexpected clinical manifestations of SARS-CoV-2 infection in humans. This lethal mouse model will also be valuable for evaluating vaccines and therapeutics for combating SARS-CoV-2 and may provide new insights into the disease pathogenesis of SARS-CoV-2.

Materials and methods

Ethics statement

The animal experiments were performed by certified staff at the Center for Animal Experiments of Wuhan University and approved by the Institutional Animal Care and Use Committee (AUP #WP2020-0819, WP2021-0007 and WP2022-0044). The protocols and procedures for handling infectious SARS-CoV-2 in an Animal Biosafety Level-III Laboratory facility were approved by the Institutional Biosafety Committee (IBC). All the samples were inactivated according to IBC-approved standard procedures for the removal of specimens from high containment.

Viruses, cells, and viral propagation

The SARS-CoV-2 wild-type (WT) strain (IVCAS 6.7512) was provided by the National Virus Resource, Wuhan Institute of Virology, Chinese Academy of Sciences [25]. The Delta variant (B.1.617.2) of SARS-CoV-2 (YJ20210707-01) and Omicron BA.1 (B.1.1.529.1) of SARS-CoV-2 (HB0000428) were provided by the Hubei Provincial Center for Disease Control and Prevention. The seed and working SARS-CoV-2 stocks were produced in Vero E6 cells (ATCC, CRL-1586) and maintained in Dulbecco's modified Eagle's medium (DMEM, Gibco) supplemented with 5% fetal bovine serum (FBS, Lonsera), 50 U/mL penicillin, and 50 μ g/mL streptomycin (Gibco). Standard plaque assays with Vero E6 cells were conducted to titrate the viral stocks. Briefly, serial 10-fold dilutions of viruses were added to monolayer Vero E6 cells for 1 hour of adsorption, and then, the inoculum was replaced with DMEM containing 1.0% methylcellulose, 50 U/mL penicillin, 50 μ g/mL streptomycin, and 5% FBS. The plates were incubated for 3 days. After evident plaques were observed, the cells were fixed with 4% paraformaldehyde for 24 h and then stained with 1% crystal violet. The plaques were counted, and the viral titers are expressed as PFU/mL.

Mouse infection and sample processing

Heterozygous B6/JGpt-H11^{em1Cin(K18-ACE2)}/Gpt mice (K18-hACE2 KI mice, #T037657, under C57BL/6J background) were purchased from GemPharmatech Co., Ltd. (Nanjing, China) (Figure 1A). The transgenic mice (HFH4-hACE2 Tg mice under C57BL/6J background) expressing the hACE2 were kindly offered by Ralph S. Baric and bred in the animal facility of the Wuhan Institute of Virology [25]. B6.Cg-Tg (K18-hACE2)2Prln/J (K18-hACE2 Tg mice, JAX #034860, under C57BL/6J background) were purchased from Jackson Laboratory (JAX lab, Bar Harbor, Maine). All the mice were maintained in individually ventilated cages (IVCs) in a specific pathogen-free (SPF) environment. For the mouse experiments, 12–18-week-old K18-hACE2 KI mice, HFH4-hACE2 Tg mice and K18-hACE2 Tg mice were anesthetized with isoflurane and intranasally (i.n.) inoculated with 50 μ L of DMEM containing the SARS-CoV-2 WT strain (2.5×10^2 or 3×10^5 PFU), Delta variant (2.5×10^2 PFU), Omicron BA.1 variant (2.5×10^2 PFU), or Omicron BA.2 variant (2.5×10^2 PFU). Mice i.n. inoculated with an equal volume of DMEM were considered as a mock control. All the mice were monitored daily for body weight changes, clinical signs of disease, and mortality throughout the study. The reduction to 80% of starting weight is our criteria for euthanasia. K18-hACE2 KI mice (at least 3 mice per group) were euthanized at 2, 4, and 6 dpi to collect

different tissue samples, which were then weighed, homogenized in PBS, and clarified by centrifugation at 5000 rpm for 5 min. The supernatant was aliquoted and stored at -80° before use.

Viral loads and hACE2 determination

For each tissue sample, 0.1 mL of clarified homogenate supernatant fluid was mixed with 0.4 mL of TRIzol LS Reagent (Invitrogen), and the total RNA was extracted according to the manufacturer's instructions. Next, first-strand cDNA was synthesized using a PrimeScript RT kit (Takara), and real-time quantitative PCR (RT-qPCR) was used to detect the presence of SARS-CoV-2 and *hACE2* distribution. In brief, the viral genome copies of SARS-CoV-2 were determined by measuring the expression of the N gene using a TaqMan RT-PCR Kit (Yeason). To accurately quantify the absolute number of SARS-CoV-2 genomes, standard curves were generated with a pCMV-N plasmid harbouring the SARS-CoV-2 N gene (Table S2). For *hACE2*, similar methods were used. All the gene numbers were normalized as the copies per milligram of tissue.

Histopathology analyses

The brains and left lobes of the lung samples were fixed with 4% paraformaldehyde for 72 hours, embedded in paraffin, and cut into 3.5 mm sections. The fixed tissue samples were used for hematoxylin – eosin (H&E) staining, modified Masson's trichrome stains, and indirect immunofluorescence assays (IFAs) to identify histopathological changes in the lung and brain samples by Wuhan Pinuofei Biological Technology company. For the IFAs, anti-*hACE2* antibody and anti-SARS-CoV/SARS-CoV-2 nucleocapsid antibody (Cat: 10108-RP01 and 40143-MM05, SinoBiological) were added as primary antibodies. The image information was collected using a Panoramic MIDI system (3DHISTECH, Budapest). Image J was used for the quantification of immunofluorescence images.

Cytokine and chemokine measurements

RNA and cDNA from lung and brain homogenates were prepared as described above. The cytokine and chemokine mRNA levels were determined using Hieff qPCR SYBR Green Master Mix (Yeason) with primers specific for *Actb*, *Tlr3*, *Tlr7*, *Tlr8*, *Ddx58*, *Irf3*, *Irf7*, *Ifna1*, *Ifna4*, *Ifnb*, *Ifnl2/3*, *Ifng*, *Il1a*, *Il1b*, *Il6*, *Il10*, *Il12a*, *Il17a*, *Il-17f*, *Il18*, *Il33*, *Tnfa*, *Tgfb*, *Ccl2*, *Ccl3*, *Ccl4*, *Ccl5*, *Ccl11*, *Cxcl1*, *Cxcl2*, *Cxcl5*, *Cxcl9*, and *Cxcl10* (Table S2). The results were normalized to *Actb* levels. The fold changes were determined using the $2^{-\Delta\Delta Ct}$ method, comparing the treated mice with uninfected controls.

Anti-SARS-CoV-2 drug evaluation

12-week-old K18-*hACE2* KI mice were infected i.n. with 2.5×10^2 PFU SARS-CoV-2 WT viruses at 0 dpi. For mAbs, mice were administrated with 10 mg/kg mAb REGN10933, 4G4, or isotype via intraperitoneal injection (i.p.) at -1 dpi. For RDV, mice were treated with 25 mg/kg Remdesivir or solvent control daily via i.p. from 0 to 5 dpi. For NMV, mice were administrated with 300 mg/kg NMV or solvent control daily by oral gavage from 0 to 5 dpi. For mRNA vaccine, mice received the first dose of mRNA vaccine intramuscularly 6 weeks prior to infection, followed by the second dose 3 weeks before infection. Infected mice were monitored for body weight changes and survival, and lung tissues were collected for evaluating viral N gene copy numbers as well as the histopathology at the indicated time points according to the methods mentioned above.

Statistical analyses

The results are shown as the mean \pm SD or mean \pm SEM. Student's *t*-tests or one-way/two-way ANOVA with Tukey's multiple comparison test were used to measure the statistical differences between samples using GraphPad Prism 8 (GraphPad Software Inc, USA). Statistically significant differences are noted as follows: *, $P < 0.05$; **, $P < 0.01$; ***, $P < 0.001$; ****, $P < 0.0001$.

For pathology score evaluation, injuries such as bleeding and edema of the entire left lung tissue can be observed by H&E staining under low microscope magnification (10 \times), the evaluation method is to observe injury distribution from 6 independent visual fields and score them according to the following criteria (injury area/total area) [61]:

- 0 points: no damage;
- 1 point: mild injury, $< 25\%$ mild influx of inflammatory cells with cuffing around vessels;
- 2 points: moderate injury, increased inflammation with $\sim 25\% - 50\%$ of the total lung involved;
- 3 points: severe inflammation involving $50\% - 75\%$ of the lung;
- 4 points: almost all lung tissue contained inflammatory infiltrates.

Acknowledgments

We are grateful to Beijing Taikang Yicai Foundation for their great support to this work. We are grateful to Dr. Kun Cai and Yongzhong Jiang, Hubei Provincial Center for Disease Control and Prevention, for providing samples and advice. We are grateful to GemPharmatech Co., Ltd. (Nanjing, China) for their great support to this work.

Disclosure statement

No potential conflict of interest was reported by the author(s).

Funding

This work was supported by the National Key R&D Program of China (2021YFF0702000 to Y.C. 2021YFC2300700 to L.Z.), National Natural Science Foundation of China (82172243, 82341061 and 82372223 to Y.C., 82272307 to K.X.), Fundamental Research Funds for the Central Universities (2042023kf1028 and 2042022dx0003 to Y.C.), Special Fund for COVID-19 Research of Wuhan University, Innovation Team Research Program of Hubei Province (2020CFA015 to K.X.), Application & Frontier Research Program of the Wuhan Government (2019020701011463 to K.X.), Advanced Customer Cultivation Project of Wuhan National Biosafety Laboratory (2021ACCP-MS10 to Y.C.), and Natural Science Foundation of Hubei Province (2023AFB201 to Z.Z.). The funders had no role in study design, data collection and analysis, decision to publish, or preparation of the manuscript.

Author contributions

Y.C., K.L., K.X., and Z.S. conceived the study and designed the experiments. Z.Z., L.Z., Q.L., Y.Z., X.T., Z.H., M.G., X.W., X.C., and S.L. performed the live SARS-CoV-2 study, animal infection experiments, and sample determinations. W.L., K.S., K.Y., J.L., Q.L., Y.Z., S.Y., Z.C., Q.X., M.D., and Z.S. assisted with the experiments. Z.Z., L.Z., and Q.L. analyzed the figures. Z.Z., L.Z., and Q.L. wrote the initial draft of the manuscript. K.X., K.L., and Y.C. revised the manuscript. All the authors read and commented on the manuscript.

Data availability statement

All data obtained for this study is included in the article.

ORCID

Yu Chen  <http://orcid.org/0000-0003-1300-4652>

References

- [1] Wu F, Zhao S, Yu B, et al. A new coronavirus associated with human respiratory disease in China. *Nature*. 2020;579(7798):265–269. doi:10.1038/s41586-020-2008-3
- [2] Zhu N, Zhang D, Wang W, et al. A novel coronavirus from patients with pneumonia in China, 2019. *N Engl J Med*. 2020;382(8):727–733. doi:10.1056/NEJMoa2001017
- [3] Zhou P, Yang XL, Wang XG, et al. A pneumonia outbreak associated with a new coronavirus of probable bat origin. *Nature*. 2020;579(7798):270–273. doi:10.1038/s41586-020-2012-7
- [4] Chen Y, Liu QY, Guo DY. Emerging coronaviruses: Genome structure, replication, and pathogenesis. *J Med Virol*. 2020;92(4):418–423. doi:10.1002/jmv.25681
- [5] Chen N, Zhou M, Dong X, et al. Epidemiological and clinical characteristics of 99 cases of 2019 novel coronavirus pneumonia in Wuhan, China: a descriptive study. *Lancet*. 2020;395(10223):507–513. doi:10.1016/S0140-6736(20)30211-7
- [6] Guan WJ, Ni ZY, Hu Y, et al. Clinical Characteristics of Coronavirus Disease 2019 in China. *N Engl J Med*. 2020;382(18):1708–1720. doi:10.1056/NEJMoa2002032
- [7] Morse JS, Lalonde T, Xu S, et al. Learning from the Past: Possible Urgent Prevention and Treatment Options for Severe Acute Respiratory Infections Caused by 2019-nCoV. *Chembiochem*. 2020;21(5):730–738. doi:10.1002/cbic.202000047
- [8] Tian S, Xiong Y, Liu H, et al. Pathological study of the 2019 novel coronavirus disease (COVID-19) through postmortem core biopsies. *Mod Pathol*. 2020;33(6):1007–1014. doi:10.1038/s41379-020-0536-x
- [9] Schaller T, Hirschbuhl K, Burkhardt K, et al. Postmortem examination of patients with COVID-19. *JAMA*. 2020;323(24):2518–2520. doi:10.1001/jama.2020.8907
- [10] Edler C, Schroder AS, Aepfelbacher M, et al. Dying with SARS-CoV-2 infection—an autopsy study of the first consecutive 80 cases in Hamburg, Germany. *Int J Legal Med*. 2020;134(4):1275–1284. doi:10.1007/s00414-020-02317-w
- [11] Huang C, Wang Y, Li X, et al. Clinical features of patients infected with 2019 novel coronavirus in Wuhan, China. *Lancet*. 2020;395(10223):497–506. doi:10.1016/S0140-6736(20)30183-5
- [12] Sia SF, Yan LM, Chin AWH, et al. Pathogenesis and transmission of SARS-CoV-2 in golden hamsters. *Nature*. 2020;583(7818):834–838. doi:10.1038/s41586-020-2342-5
- [13] Imai M, Iwatsuki-Horimoto K, Hatta M, et al. Syrian hamsters as a small animal model for SARS-CoV-2 infection and countermeasure development. *Proc Natl Acad Sci U S A*. 2020;117(28):16587–16595. doi:10.1073/pnas.2009799117
- [14] Hu Y, Liu M, Qin H, et al. Artemether, Artesunate, Arteannuin B, Echinatin, Licochalcone B and Andrographolide Effectively Inhibit SARS-CoV-2 and Related Viruses In Vitro. *Front Cell Infect Microbiol*. 2021;11:680127. doi:10.3389/fcimb.2021.680127
- [15] Xu L, Yu DD, Ma YH, et al. COVID-19-like symptoms observed in Chinese tree shrews infected with SARS-CoV-2. *Zool Res*. 2020;41(5):517–526. doi:10.24272/j.issn.2095-8137.2020.053
- [16] Woolsey C, Borisevich V, Prasad AN, et al. Establishment of an African green monkey model for COVID-19 and protection against re-infection. *Nat Immunol*. 2021;22(1):86–98. doi:10.1038/s41590-020-00835-8
- [17] Rockx B, Kuiken T, Herfst S, et al. Comparative pathogenesis of COVID-19, MERS, and SARS in a nonhuman primate model. *Science*. 2020;368(6494):1012–1015. doi:10.1126/science.abb7314
- [18] Shang J, Ye G, Shi K, et al. Structural basis of receptor recognition by SARS-CoV-2. *Nature*. 2020;581(7807):221–224. doi:10.1038/s41586-020-2179-y
- [19] Israelow B, Song E, Mao T, et al. Mouse model of SARS-CoV-2 reveals inflammatory role of type I interferon signaling. *J Exp Med*. 2020;217(12). doi:10.1084/jem.20201241

- [20] Rathnasinghe R, Strohmeier S, Amanat F, et al. Comparison of transgenic and adenovirus hACE2 mouse models for SARS-CoV-2 infection. *Emerg Microbes Infect.* 2020;9(1):2433–2445. doi:10.1080/22221751.2020.1838955
- [21] Zheng J, Wong LR, Li K, et al. COVID-19 treatments and pathogenesis including anosmia in K18-hACE2 mice. *Nature.* 2021;589(7843):603–607. doi:10.1038/s41586-020-2943-z
- [22] Moreau GB, Burgess SL, Sturek JM, et al. Evaluation of K18-hACE2 Mice as a Model of SARS-CoV-2 Infection. *Am J Trop Med Hyg.* 2020;103(3):1215–1219. doi:10.4269/ajtmh.20-0762
- [23] Liu X, Zaid A, Freitas JR, et al. Infectious clones produce SARS-CoV-2 that causes severe pulmonary disease in infected K18-human ACE2 mice. *mBio.* 2021;12(2).
- [24] Yinda CK, Port JR, Bushmaker T, et al. K18-hACE2 mice develop respiratory disease resembling severe COVID-19. *PLoS Pathog.* 2021;17(1):e1009195. doi:10.1371/journal.ppat.1009195
- [25] Jiang RD, Liu MQ, Chen Y, et al. Pathogenesis of SARS-CoV-2 in transgenic mice expressing human angiotensin-converting enzyme 2. *Cell.* 2020;182(1):50–58.e8. doi:10.1016/j.cell.2020.05.027
- [26] Golden JW, Cline CR, Zeng X, et al. Human angiotensin-converting enzyme 2 transgenic mice infected with SARS-CoV-2 develop severe and fatal respiratory disease. *JCI Insight.* 2020;5(19). doi:10.1172/jci.insight.142032
- [27] Winkler ES, Bailey AL, Kafai NM, et al. SARS-CoV-2 infection of human ACE2-transgenic mice causes severe lung inflammation and impaired function. *Nature Immunol.* 2020;21(11):1327–1335. doi:10.1038/s41590-020-0778-2
- [28] Oladunni FS, Park JG, Pino PA, et al. Lethality of SARS-CoV-2 infection in K18 human angiotensin-converting enzyme 2 transgenic mice. *Nat Commun.* 2020;11(1):6122. doi:10.1038/s41467-020-19891-7
- [29] Song E, Zhang C, Israelow B, et al. Neuroinvasion of SARS-CoV-2 in human and mouse brain. *J Exp Med.* 2021;218(3). doi:10.1084/jem.20202135
- [30] Kumari P, Rothan HA, Natekar JP, et al. Neuroinvasion and Encephalitis Following Intranasal Inoculation of SARS-CoV-2 in K18-hACE2 Mice. *Viruses.* 2021;13(1):132. doi:10.3390/v13010132
- [31] Golden JW, Zeng X, Cline CR, et al. Human convalescent plasma protects K18-hACE2 mice against severe respiratory disease. *J Gen Virol.* 2021;102(5). doi:10.1099/jgv.0.001599
- [32] Caceres CJ, Cardenas-Garcia S, Carnaccini S, et al. Efficacy of GC-376 against SARS-CoV-2 virus infection in the K18 hACE2 transgenic mouse model. *Sci Rep.* 2021;11(1):9609. doi:10.1038/s41598-021-89013-w
- [33] Sun SH, Chen Q, Gu HJ, et al. A mouse model of SARS-CoV-2 infection and pathogenesis. *Cell Host Microbe.* 2020;28(1):124–133.e4. doi:10.1016/j.chom.2020.05.020
- [34] Bao L, Deng W, Huang B, et al. The pathogenicity of SARS-CoV-2 in hACE2 transgenic mice. *Nature.* 2020;583(7818):830–833. doi:10.1038/s41586-020-2312-y
- [35] Dinnon KH, 3rd, Leist SR, Schafer A, et al. A mouse-adapted model of SARS-CoV-2 to test COVID-19 countermeasures. *Nature.* 2020;586(7830):560–566. doi:10.1038/s41586-020-2708-8
- [36] Gu H, Chen Q, Yang G, et al. Adaptation of SARS-CoV-2 in BALB/c mice for testing vaccine efficacy. *Science.* 2020;369(6511):1603–1607. doi:10.1126/science.abc4730
- [37] Sun S, Gu H, Cao L, et al. Characterization and structural basis of a lethal mouse-adapted SARS-CoV-2. *Nat Commun.* 2021;12(1):5654. doi:10.1038/s41467-021-25903-x
- [38] Leist SR, Dinnon KH, 3rd, Schafer A, et al. A mouse-adapted SARS-CoV-2 induces acute lung injury and mortality in standard laboratory mice. *Cell.* 2020;183(4):1070–1085.e12. doi:10.1016/j.cell.2020.09.050
- [39] McCray PB, Jr., Pewe L, Wohlford-Lenane C, et al. Lethal infection of K18-hACE2 mice infected with severe acute respiratory syndrome coronavirus. *J Virol.* 2007;81(2):813–821. doi:10.1128/JVI.02012-06
- [40] Gan ES, Syenina A, Linster M, et al. A mouse model of lethal respiratory dysfunction for SARS-CoV-2 infection. *Antiviral Res.* 2021;193:105138. doi:10.1016/j.antiviral.2021.105138
- [41] Abdelnabi R, Foo CS, Zhang X, et al. The omicron (B.1.1.529) SARS-CoV-2 variant of concern does not readily infect Syrian hamsters. *Antiviral Res.* 2022;198:105253. doi:10.1016/j.antiviral.2022.105253
- [42] Ying B, Scheaffer SM, Whitener B, et al. Boosting with variant-matched or historical mRNA vaccines protects against Omicron infection in mice. *Cell.* 2022;185(9):1572–1587.e11. doi:10.1016/j.cell.2022.03.037
- [43] Shuai HP, Chan JFW, Hu BJ, et al. Attenuated replication and pathogenicity of SARS-CoV-2 B.1.1.529 Omicron. *Nature.* 2022;603(7902):693–699. doi:10.1038/s41586-022-04442-5
- [44] Halfmann PJ, Iida S, Iwatsuki-Horimoto K, et al. SARS-CoV-2 Omicron virus causes attenuated disease in mice and hamsters. *Nature.* 2022;603(7902):687–692. doi:10.1038/s41586-022-04441-6
- [45] Chen Y, Liu Q, Zhou L, et al. Emerging SARS-CoV-2 variants: Why, how, and what's next? *Cell Insight.* 2022;1(3):100029. doi:10.1016/j.cellin.2022.100029
- [46] Zhang L, Zhou L, Bao L, et al. SARS-CoV-2 crosses the blood-brain barrier accompanied with basement membrane disruption without tight junctions alteration. *Signal Transduct Target Ther.* 2021;6(1):337. doi:10.1038/s41392-021-00719-9
- [47] Liu QY, Zhao HY, Li ZQ, et al. Broadly neutralizing antibodies derived from the earliest COVID-19 convalescents protect mice from SARS-CoV-2 variants challenge. *Signal Transduction and Targeted Therapy.* 2023;8:347. doi:10.1038/s41392-023-01615-0
- [48] Corbett KS, Edwards DK, Leist SR, et al. SARS-CoV-2 mRNA vaccine design enabled by prototype pathogen preparedness. *Nature.* 2020;586(7830):567–571. doi:10.1038/s41586-020-2622-0
- [49] Jeong JH, Chokkakula S, Min SC, et al. Combination therapy with nirmatrelvir and molnupiravir improves the survival of SARS-CoV-2 infected mice. *Antiviral Res.* 2022;208:105430. doi:10.1016/j.antiviral.2022.105430
- [50] Sun J, Zhuang Z, Zheng J, et al. Generation of a broadly useful model for COVID-19 pathogenesis, vaccination, and treatment. *Cell.* 2020;182(3):734–743.e5. doi:10.1016/j.cell.2020.06.010
- [51] Ueno M, Iwata-Yoshikawa N, Matsunaga A, et al. Isolation of human monoclonal antibodies with neutralizing activity to a broad spectrum of SARS-CoV-2 viruses including the Omicron variants. *Antiviral*

- Res. 2022;201:105297. doi:10.1016/j.antiviral.2022.105297
- [52] Baum A, Ajithdoss D, Copin R, et al. REGN-COV2 antibodies prevent and treat SARS-CoV-2 infection in rhesus macaques and hamsters. *Science*. 2020;370(6520):1110–1115. doi:10.1126/science.abe2402
- [53] Onodera T, Kita S, Adachi Y, et al. A SARS-CoV-2 antibody broadly neutralizes SARS-related coronaviruses and variants by coordinated recognition of a virus-vulnerable site. *Immunity*. 2021;54(10):2385–2398.e10. doi:10.1016/j.immuni.2021.08.025
- [54] Uraki R, Kiso M, Iida S, et al. Characterization and antiviral susceptibility of SARS-CoV-2 Omicron BA.2. *Nature*. 2022;607(7917):119–127. doi:10.1038/s41586-022-04856-1
- [55] Najjar-Debbiny R, Gronich N, Weber G, et al. Effectiveness of Paxlovid in reducing severe coronavirus disease 2019 and mortality in high-risk patients. *Clin Infect Dis*. 2023;76(3):E342–E349. doi:10.1093/cid/ciac443
- [56] Spinner CD, Gottlieb RL, Criner GJ, et al. Effect of remdesivir vs standard care on clinical status at 11 days in patients with moderate COVID-19 a randomized clinical trial. *JAMA*. 2020;324(11):1110–1057. doi:10.1001/jama.2020.11856
- [57] Hikmet F, Méar L, Edvinsson Å, et al. The protein expression profile of ACE2 in human tissues. *Mol Syst Biol*. 2020;16(7). doi:10.15252/msb.20209610
- [58] Hamming I, Timens W, Bulthuis MLC, et al. Tissue distribution of ACE2 protein, the functional receptor for SARS coronavirus. A first step in understanding SARS pathogenesis. *J Pathol*. 2004;203(2):631–637. doi:10.1002/path.1570
- [59] Carson MJ, Doose JM, Melchior B, et al. CNS immune privilege: hiding in plain sight. *Immunol Rev*. 2006;213:48–65. doi:10.1111/j.1600-065X.2006.00441.x
- [60] Turrin NP, Rivest S. Molecular and cellular immune mediators of neuroprotection. *Mol Neurobiol*. 2006;34(3):221–242. doi:10.1385/MN:34:3:221
- [61] Ai L, Li Y, Zhou L, et al. Lyophilized mRNA-lipid nanoparticle vaccines with long-term stability and high antigenicity against SARS-CoV-2. *Cell Discov*. 2023;9(1):9. doi:10.1038/s41421-022-00517-9